Dalton Transactions

ROYAL SOCIETY OF CHEMISTRY

PAPER

View Article Online
View Journal | View Issue

Cite this: *Dalton Trans.*, 2025, **54**, 8133

Magnetism and electrical and thermal transport in the natural $Fe_{1-x}Mn_xWO_4$ (x = 0.2) mineral from Potosí, Bolivia†

Dmytro Skachko, [a] Bohdan Kundys, [b] Volodymyr Levytskyi, [a] Esteban Zuñiga-Puelles, [a] Andreas Leithe-Jasper [c] and Roman Gumeniuk *[a]

Received 11th February 2025,
Accepted 25th February 2025

DOI: 10.1039/d5dt00332f

rsc.li/dalton

The composition of a natural single crystalline specimen from the province of Potosí in Bolivia is found to be $Fe_{0.8}Mn_{0.2}WO_4$. It crystallizes with the primitive monoclinic $NiWO_4$ structure type [space group $P2/c$, a = 4.74751(6) Å, b = 5.71335(7) Å, c = 4.96847(5) Å, β = 90.15(1)°]. Magnetic susceptibility and specific heat capacity measurements indicated that the mineral undergoes multiple magnetic transitions: $T_{N1} \approx T_{N1}^{C_p}$ = 67(1) K, T_{N2} = 28(3) K, and $T_{N2}^{C_p}$ = 8(1) K. The reduced magnetic entropy of $\approx R \ln 3$ upon the high-temperature antiferromagnetic ordering suggests the failure of the simplified LS-coupling scheme in the description of the magnetism. $Fe_{0.8}Mn_{0.2}WO_4$ is characterized by enlarged electrical resistivity showing an exponential decrease with temperature for T > 300 K, from which an energy gap of 310 meV is deduced. The well-pronounced maximum occurring in the phononic thermal conductivity just below the T_{N1} is described by the Debye–Callaway model, indicating the dominance of phonon scattering on defects as well as umklapp processes.

1 Introduction

Mixed $Fe_{1-x}Mn_xWO_4$ tungstates play an important role in the development of supercapacitors and photoluminescent-, photocatalytic- and electrode materials for lithium-ion batteries.[1–8] As a result, investigations into their magnetic, electrochemical and photoluminescence properties have become a prominent area of scientific inquiry. Nevertheless, despite the increased interest in this class of materials, several crystallochemical, magnetic, thermodynamic points remain less clear.

Given that both the ternary $FeWO_4$ (ferberite) and $MnWO_4$ (huebnerite) as well as quaternary $Fe_{1-x}Mn_xWO_4$ (wolframite) tungstates occur as natural minerals, their crystal structures have been the subject of extensive investigation since the nineteenth century.[9] They were shown to crystallize with a monoclinic (space group $P2/c$) wolframite ($NiWO_4$) structure type.[9,10] Such an arrangement foresees d-elements to reside within the condensed distorted [O_6] octahedra, a hypothesis that is both crystallographically and chemically plausible. Nevertheless, the existence of a small monoclinic distortion (angle $\beta \approx 90°$) has prompted a number of reinvestigations.[1,4,9] One of the most recent ones confirming the questionable β found that the $FeWO_4$ structure is indeed characterized by partial occupancy of the normally empty [O_4]-tetrahedral voids.[4] Obviously, the nature of the chemical disorder in quaternary $Fe_{1-x}Mn_xWO_4$ remains unknown due to the neighboring positions of the d-element constituents in the periodic table. Importantly, no phase transition for the natural $FeWO_4$ is observed up to 20 GPa.[1]

Magnetic measurements indicated that $FeWO_4$ orders antiferromagnetically at T_N = 75 K and reveals anisotropic properties due to the magneto-crystalline anisotropy of the Fe^{2+} ions. Such a behavior is explained by the super-exchange interactions occurring *via* O^{2-}-ions along distinct paths between neighboring Fe^{2+} ions.[11] The change of the magnetic entropy $\Delta S_{mag} = R \ln 5$ (gas constant R = 8.314 J mol^{-1} K^{-1}) for $FeWO_4$ upon the transition was deduced from the specific heat measurements and it is again in line with the 2+ oxidation state of iron ions (*i.e.*, it corresponds to the total spin angular momentum S = 2).[9] On the other hand, $MnWO_4$ is characterized by a much more complex magnetic structure, including three transitions at T_N of 13.5 K, 12.3 K and 8 K, respectively. The low temperature antiferromagnetic phases were shown to

[a]*Institut für Experimentelle Physik, TU Bergakademie Freiberg, Leipziger Straße 23, 09599 Freiberg, Germany. E-mail: roman.gumeniuk@physik.tu-freiberg.de*
[b]*Université de Strasbourg, CNRS, Institut de Physique et Chimie des Matériaux de Strasbourg, UMR 7504, Strasbourg F-67000, France*
[c]*Max-Planck-Institut für Chemische Physik fester Stoffe, Nöthnitzer Straße 40, 01187 Dresden, Germany*

†Electronic supplementary information (ESI) available. CCDC 2425342. For ESI and crystallographic data in CIF or other electronic format see DOI: https://doi.org/10.1039/d5dt00332f

possess incommensurately modulated structures.[12,13] Interestingly, both quaternary $Fe_{1-x}Mn_xWO_4$ ferberite and hubnerite always reveal magnetic behavior reminiscent of those of $MnWO_4$. Some attempts to construct magnetic phase diagrams for them are made in ref. 11 and 14.

The reported electrical resistivities [$\rho(T)$] for both $FeWO_4$ and $MnWO_4$ are large, varying in the range of Ω m–kΩ m, which are characterized by an exponential decrease with temperature. The increased conductivity in $FeWO_4$ at RT is believed to be related to the presence of a small admixture of Fe^{3+} ions, which triggers electron hopping along and between the chains in the [001]-direction.[15] On the other hand, higher $\rho(T)$ in $MnWO_4$ is explained by small and large polaron hopping for LT- and HT-regimes, respectively.[16] Now, in mixed $Fe_{1-x}Mn_xWO_4$ tungstates, characterized by the presence of Mn^{2+} ions, it is believed that the latter do not block the electron hopping paths and thus, the interchain electron transfer is possible.[15]

The Seebeck coefficients [$\alpha(T)$] of $FeWO_4$ [4,7,15,17] and $MnWO_4$ [16] are large and positive in the whole studied temperature range, assuming the dominance of hole-like conduction mechanisms. The decrease in the values of $\alpha(T)$ (*i.e.*, they vary between 140 μV K^{-1} and 350 μV K^{-1} at RT depending on the synthesis route) in $FeWO_4$ is explained by the increase of Fe^{3+}-impurity ion concentration.[4]

The energy band gaps of ≈2 eV (ref. 8 and 18–20) and ≈2.6 eV (ref. 7, 18 and 20) for $FeWO_4$ and $MnWO_4$, respectively, were estimated by spectroscopic measurements and further confirmed by the simulations within density functional theory. The high-pressure studies revealed that the energy gap of $FeWO_4$ can be suppressed to 1.56 eV at 16 GPa (ref. 1) and to 2.08 eV at 10 GPa for $MnWO_4$.[21]

Magnetic studies have been conducted on quaternary natural $Fe_{1-x}Mn_xWO_4$ ($x \approx 0.2$) minerals sourced from Portugal and Mexico.[22] However, a comprehensive analysis of their electrical and thermal transport properties remains unavailable. In this work, we provide a combined investigation of the structural and physical properties of the $Fe_{0.8}Mn_{0.2}WO_4$ single-crystalline specimen sourced from the Potosí province in Bolivia.

2 Experimental

The studied specimen is a natural single crystal of the $Fe_{1-x}Mn_xWO_4$ composition belonging to the group of wolframite minerals and originating from the Potosí province in Bolivia, which is known for the excellent quality of such minerals.[23]

The specimen was characterized by powder X-ray diffraction performed using a Huber G670 Guinier camera ($CuK_{\alpha 1}$ radiation, λ = 1.54056 Å). Phase analysis was performed using the WinXpow software package[24] and Rietveld refinement was performed using WinCSD.[25] Single-crystal diffraction [SCXRD, a STOE STADIVARI diffractometer (MoKα radiation, λ = 0.71073 Å) equipped with a Dectris Pilatus300K detector] was performed on a crystal mechanically extracted from the crushed sample.

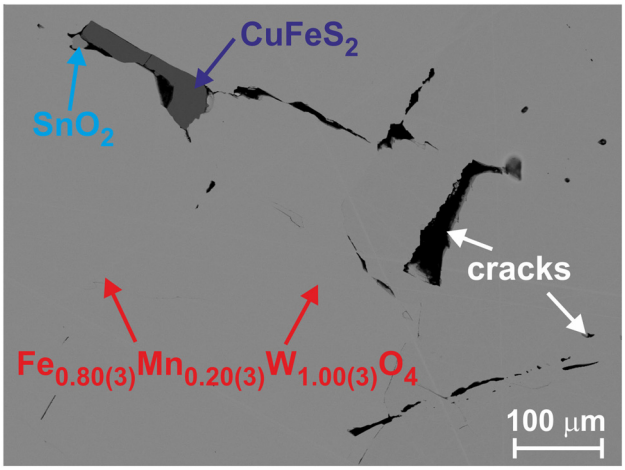

Fig. 1 Backscattered electron image of $Fe_{0.8}Mn_{0.2}WO_4$ with the identification of phases.

The supplementary crystallographic data for $Fe_{0.8}Mn_{0.2}WO_4$ are deposited under CCDC 2425342.†

The surface of the polished wolframite embedded in a conductive resin was investigated using a scanning electron microscope (SEM) (Jeol JSM − 7800F) equipped with an energy dispersive X-ray spectrometer (EDXS) Quantax 400 EDXS system from Bruker. Such an analysis indicated the (Fe,Mn) : W relationship in the main phase to be 1 : 1 with an oxygen content of ≈70 at%. Recalculating further the Fe and Mn contents, we deduced the $Fe_{0.80(3)}Mn_{0.20(3)}W_{1.00(3)}O_4$ chemical composition for the studied wolframite. Besides the main phase, the investigated specimen contained an admixture of SnO_2 and $CuFeS_2$ (Fig. 1), which was not visible in the measured PXRD patterns.

Temperature (1.8–300 K) and magnetic field (0–7 T) dependencies of magnetic susceptibility, specific heat capacity and thermal conductivity were measured by the corresponding options of DynaCool-12 from Quantum Design. High temperature (450–600 K) electrical resistivity and Seebeck coefficients were obtained using an ULVAC ZEM-3 device. Due to the highly insulating nature of the sample for T < 450 K, electrical resistivity was additionally measured using an AC method at 100 kHz with an Agilent Precision LCR meter, Model E4980A.

3 Results and discussion

3.1 Crystal structure

All reflections collected for $Fe_{0.8}Mn_{0.2}WO_4$ from the single crystal XRD experiment were indexed within the monoclinic lattice with the unit cell parameters a = 4.7466(9) Å, b = 5.711 (1) Å, c = 4.969(1) Å and β = 90.21(3)°. The analysis of the extinction conditions indicated $l = 2n$ for $h0l$ and $00l$ indices and thus, two possible space groups (SG) $P2/c$ or Pc. In the first step we have chosen the centrosymmetric one to find a struc-

tural model. By applying direct methods four atomic positions were located as shown in Table 1. The preliminary refinement cycle converged with a low reliability factor R_F = 0.033, indicating the correctness of the obtained model. Performing further extinction correction and refining anisotropic displacement parameters (ADP), R_F was reduced to 0.014. Crystallographic details of this refinement together with the final values of atomic coordinates and equivalent displacement parameters are collected in Table 1. The obtained ADPs are shown in Table 2. Since Fe and Mn are neighboring elements in the periodic table, reasonable refinement of their statistical mixture is rather impossible. Therefore, the composition of the crystal was fixed to the results from EDX analysis.

Table 1 Crystallographic data for $Fe_{0.8}Mn_{0.2}WO_4$ (SG *P2/c*)

Method	Single crystal	Powder
Unit cell parameters[a]		
a (Å)	4.74751(6)	
b (Å)	5.71335(7)	
c (Å)	4.96847(5)	
β (°)	90.15(1)	
V (Å^3)	134.76(2)	
Calculated density ρ (g cm^{-3})	7.48(1)	
Radiation, λ (Å)	MoK_α, 0.71073	Cu$K_{\alpha1}$, 1.54056
Absorption coeff. (mm^{-1})	50.40	122.1
Scan step (°); N (images)	1° (ω-scans); 1414	0.005
Maximal 2Θ (°)	76.47	100.41
Minimal h, k, l	−6, −9, −8	0, 0, −4
Maximal h, k, l	8, 9, 8	4, 5, 5
Crystal size, μm^3	20 × 40 × 96	
Absorption correction	Multiscan	
T_{max}/T_{min}	0.376/0.187	
N (hkl) measured	6523	156
N (hkl) unique	739	
R_{int}/R_σ	0.066/0.026	
N (hkl) observed	6316	
Observation criterion	$F(hkl) \geq 4\sigma(F)$	
Refined parameters	33	22
Extinction coefficient	0.0389(8)	
Goodness of fit, S	1.03	1.01
$R_F(R_I)$; $R_W(R_P)$	0.014/0.015	0.056; 0.103
Residual peaks (e$^-$ Å^{-3})	−0.41/0.50	−0.57/0.73
M in 2f (1/2 y 3/4), y, $B_{eq/iso}$ [b]	0.3253(2), 0.70(1)	0.3278(3), 1.05(1)
$d_{(M-2O1)}$, $d_{(M-2O2)}$	2.069(3), 2.140(3)	2.064(4), 2.171(5)
$d_{(M-2O2)}$, $d_{(M-2M)}$	2.190(3), 3.1869(8)	2.248(5), 3.169(2)
W in 2e (0 y 1/4), y, $B_{eq/iso}$	0.18021(4), 0.484(4)	0.1798(1), 1.13(1)
$d_{(W-2O2)}$, $d_{(W-2O1)}$	1.789(3), 1.913(3)	1.736(4), 1.909(5)
$d_{(W-2O1)}$, $d_{(W-2W)}$	2.129(3), 3.2267(2)	2.142(4), 3.2237(5)
O1 in 4g (xyz), x, y	0.2129(6), 0.1059(5)	0.2119(9), 0.1101(7)
z, $B_{eq/iso}$	0.9351(5), 0.70(4)	0.934(1), 0.90(2)
O2 in 4g (xyz), x, y	0.2536(6), 0.3757(5)	0.2363(9), 0.3830(8)
z, $B_{eq/iso}$	0.3933(6), 0.75(5)	0.379(1), 0.96(2)

[a] Obtained from PXRD and used for single crystal refinement. [b] M is a statistical mixture of (0.8Fe + 0.2Mn) in accordance with EDX analysis.

Table 2 Anisotropic displacement parameters (B_{ij}, Å^2) for $Fe_{0.8}Mn_{0.2}WO_4$

Atom	B_{11}	B_{22}	B_{33}	B_{12}	B_{13}	B_{23}
M[a]	0.69(2)	0.77(2)	0.65(2)	0	0.02(2)	0
W	0.594(7)	0.431(6)	0.427(6)	0	−0.015(4)	0
O1	0.80(8)	0.69(8)	0.62(7)	−0.19(7)	0.04(6)	0.00(6)
O2	0.59(8)	0.86(8)	0.81(8)	−0.15(6)	−0.10(6)	−0.08(7)

[a] M is a statistical mixture of (0.8Fe + 0.2Mn) in accordance with EDX analysis.

As one can see from Table 2, the B_{11} displacement parameter for the heavy W-atom is by a factor of ≈1.4 larger than B_{22} and B_{33}. This fact together with the partial occupancy by Fe and W of the additional tetrahedral voids reported in ref. 4 prompted us to check the possibility of the latter scenario in the studied wolframite. For these purposes, we performed differential Fourier synthesis before refining ADPs. It indicated an additional electronic density of +2.85 e$^-$ Å^{-3} localized at the 4g [0.041(2) 0.176(2) 0.2470(6)] crystallographic site, which is just a split position to the available W in 2e (Table 1). This observation brought us to the conclusion that the model proposed in ref. 4 cannot be applied to the natural wolframite. We assume instead that the enlarged B_{11} for $Fe_{0.8}Mn_{0.2}WO_4$ is most probably due to mechanical stress in the microcrystal appearing after crushing the initial sample – an effect discussed in more detail elsewhere.[26–29]

The obtained structural model from single crystal XRD was used to refine the powder XRD data, which converged with low reliability factors. The atomic coordinates and displacement parameters are collected in Table 1. The experimental, theoretical and differential profiles for it are depicted in Fig. 2. Importantly, the hkl reflections with $h \neq 0$ and $l \neq 0$ are found to reveal a clear split. It is visible in the inset to Fig. 2, where some of these peaks are presented in comparison with the (230) one. Such an indication of the monoclinic distortion can sometimes remain invisible, as it is the case in the sample observed in ref. 4.

The refined unit cell parameters (Table 1) agree well with the predictions made for $Fe_{1-x}Mn_xWO_4$ tungstates on the basis of the XRD investigations of some natural minerals.[6] The strongest deviation of ≈0.2% is observed for the a-parameter

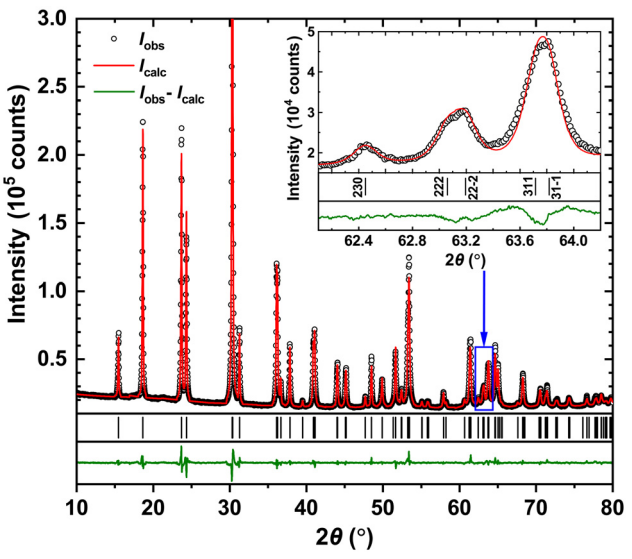

Fig. 2 Powder XRD patterns for $Fe_{0.8}Mn_{0.2}WO_4$. Inset: indexing of the selected reflections. A clear split is visible for those with $h \neq 0$ and $l \neq 0$, confirming the monoclinic distortion.

and thus, deducing from Fig. 5 in ref. 6, the Mn-content for the compound studied here would be x = 0.38. However, one can see from the study[6] that the data obtained for x < 0.5 (*e.g.*, available in ref. 4, 30 and 31) strongly deviate from the proposed linear $x(V)$-dependence. For this reason, the higher Mn-content in our mineral is rather unlikely.

The refined interatomic distances in the crystal structure of $Fe_{0.8}Mn_{0.2}WO_4$ (Table 1) agree well with the sums of ionic radii of the corresponding ions [$r_{(Fe^{2+})}$ = 0.82 Å, $r_{(Mn^{2+})}$ = 0.91 Å, and $r_{(O^{2-})}$ = 1.32 Å].[32] The maximal shortenings of Fe–O and W–O contacts do not exceed 3.3% and 7.8%, respectively, and agree well with the earlier reports.[4,31]

The structural peculiarities of the $NiWO_4$ type are widely discussed in the literature.[4,10,31,33] It is considered as consisting of [FeO_6]- (distorted due to the Jahn–Teller effect) and [WO_6]-octahedra sharing their edges and forming zigzag chains along the [001] direction. Also, along the [100] direction, filled octahedra alternate with the empty ones, thus possessing common trigonal faces and being organized in columns (Fig. 3a). Such a close packing of octahedra gives rise to interstitial tetrahedral voids. They can become partially filled (Fig. 3b), as has been shown on the basis of combined single crystal XRD, TEM and SEM studies in ref. 4. Alternatively, one could consider the crystal structure of $FeWO_4$ to be consisting of trigonal puckered nets formed by oxygen atoms extending in the *bc*-plane and being at $x \approx 0.25$ and 0.75, respectively (Fig. 3c). In the free space in-between, the planar trigonal nets (not shown in Fig. 3c) formed by W^{6+} (x = 0) and Fe^{2+} (x = 1/2) are incorporated. Such a layered presentation, however, has less chemical meaning due to the absence of bonding Fe–Fe, W–W and O–O contacts in the studied structure.

3.2 Magnetic susceptibility

The temperature dependence of reciprocal magnetic susceptibility $\chi^{-1}(T)$ for $Fe_{0.8}Mn_{0.2}WO_4$ is depicted in Fig. 4. In the T-range of 130–300 K, it perfectly fits the Curie–Weiss law $\chi^{-1} = (T - \Theta_{CW})/C$. The Weiss temperature Θ_{CW} = −19(1) K and the effective magnetic moment $\mu_{eff} = \sqrt{3k_B C/N_A\mu_0} = 5.4(1)\mu_B$ obtained from such a fit agree well with those reported for pure $FeWO_4$.[34,35] The somewhat smaller Θ_{CW} value [−19(1) K instead of −27 K] can be explained by the relatively narrow T-range in which our fit was performed.

With the lowering temperature, $Fe_{0.8}Mn_{0.2}WO_4$ undergoes an antiferromagnetic (AF) transition at T_{N1} = 67(1) K, in agreement with ref. 36, and further changes its magnetic structure at T_{N2} = 28(3) K. As one can see from inset a to Fig. 4, the value of T_{N1} nicely fits that of T_N from Mn-content dependence, confirming the correctness of the chemical composition (established from EDX) of the studied mineral. Additionally, almost no and very weak field dependencies are observed for T_{N1} and T_{N2}, respectively (inset b to Fig. 4). All these findings agree well with the earlier reports about complex magnetic phase formation in $Fe_{1-x}Mn_xWO_4$, which is caused by the various superexchange couplings between adjacent Mn–Mn, Fe–Fe, and Mn–Fe-ions *via* one or two intervening oxygen ions.[1,11,34]

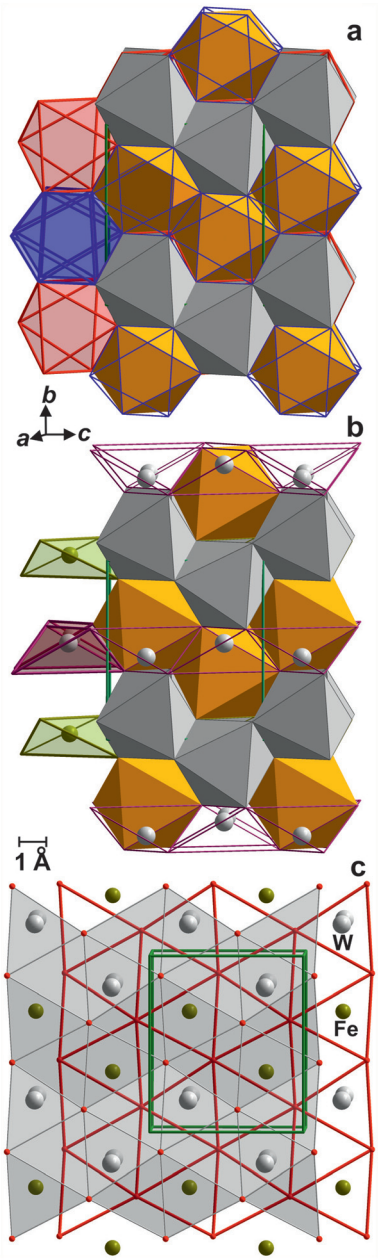

Fig. 3 (a) Arrangement of filled and empty octahedra in $FeWO_4$ ($NiWO_4$ type). (b) Structural model with partially filled tetrahedra (the full occupancy is shown) proposed for $FeWO_4$ in ref. 4. (c) Arrangement of the puckered trigonal nets W^{6+} and Fe^{2+} ions in-between (for more details, see the text).

3.3 Specific heat

The temperature dependence of specific heat capacity $c_p(T)$ for $Fe_{0.8}Mn_{0.2}WO_4$ in different magnetic fields in comparison with the synthetic ternary $FeWO_4$ and phonon reference compound $ZnWO_4$ (both these data are taken from ref. 9) is depicted in Fig. 5. In agreement with magnetic susceptibility (inset b to Fig. 4) no suppression of AF with increasing field is observed. Also, expectedly, the anomaly due to the antiferromagnetic

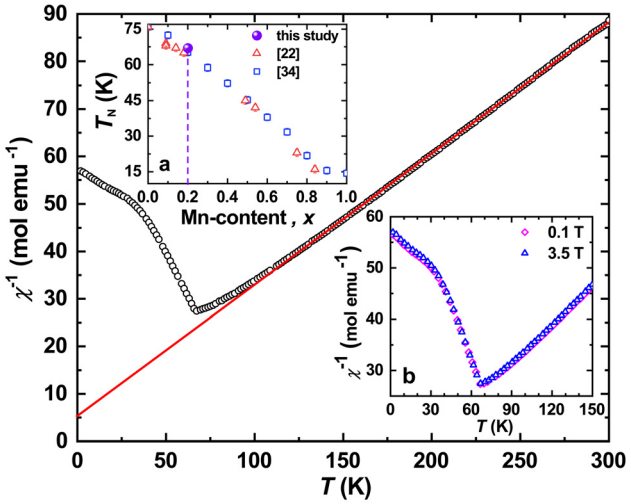

Fig. 4 Temperature dependence of reciprocal magnetic susceptibility for $Fe_{0.8}Mn_{0.2}WO_4$ ($\mu_0 H$ = 3.5 T) together with the Curie–Weiss fit (red line). Inset a: dependence of critical Néel-temperatures (T_N) *versus* Mn content (x) in $Fe_{1-x}Mn_xWO_4$. Inset b: temperature dependence of reciprocal magnetic susceptibility for $Fe_{0.8}Mn_{0.2}WO_4$ in different magnetic fields.

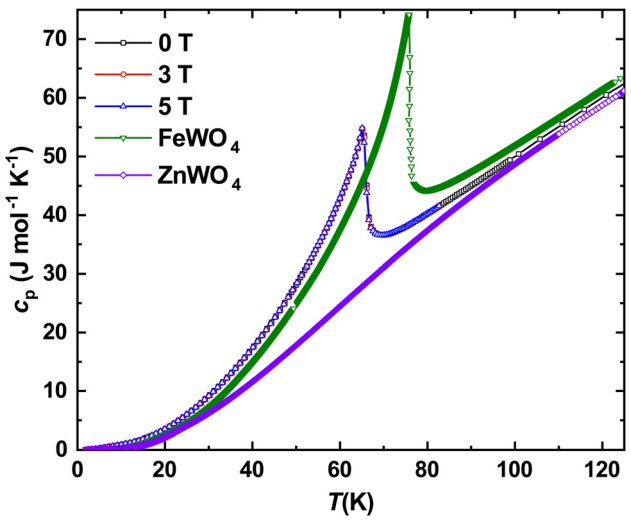

Fig. 5 Temperature dependencies of specific heat capacity in different magnetic fields for $Fe_{0.8}Mn_{0.2}WO_4$ together with the literature data for $FeWO_4$ and $ZnWO_4$.[9]

ordering at $T_{N1}^{c_p}$ = 66(1) K in the studied mineral is shifted towards a lower T (inset to Fig. 4).

Subtracting further the phonon reference, we obtained the electronic specific heat for $Fe_{0.8}Mn_{0.2}WO_4$. Presenting it in $c_{el}/T(T)$ mode and integrating it, we obtained the temperature evolution of the magnetic entropy $\Delta S_{mag} = \int_{T_1}^{T_2} (c_{el}/T)dT$. As one can see from Fig. 6, a value slightly larger than R ln3 can be reached upon the transition. Obviously, it is much lower than the theoretical expectations for Fe^{2+} (S = 2) or Fe^{3+} (S = 5/2) ions given as $\Delta S_{mag} = R\ln(2S+1) = R\ln 5$ and $R\ln 6$, respectively. On the other hand, assuming the influence of the crystal electric

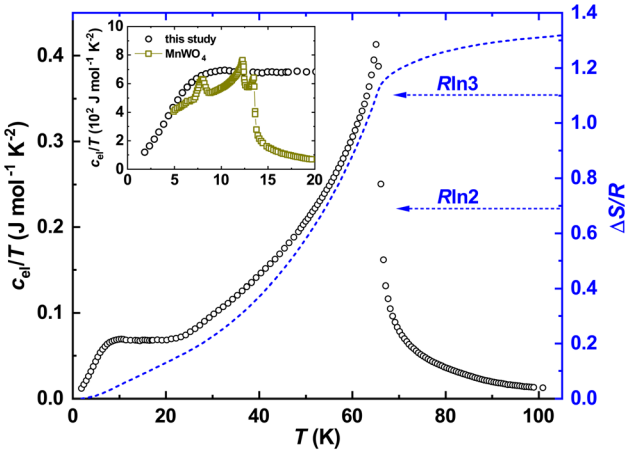

Fig. 6 Temperature dependence of the electronic specific heat of $Fe_{0.8}Mn_{0.2}WO_4$ in the $c_{el}/T(T)$ presentation (left black scale) together with the temperature evolution of the magnetic entropy near an antiferromagnetic transition. Inset: low-temperature dependencies of $c_{el}/T(T)$ for $Fe_{0.8}Mn_{0.2}WO_4$ together with the literature data for $MnWO_4$.[37] The latter were divided by 20 for better visualization.

field effect on Fe-ions, and thus electronic configurations with S = 1 or 3/2, one could also deduce the entropies R ln3 and R ln4, respectively. It is noteworthy that the reduced total spin angular momenta should also indicate much lower effective magnetic moments disagreeing with our experiment. All these hints towards the failure of the simplified classical LS-coupling scheme in the description of the complex magnetic behavior in $Fe_{0.8}Mn_{0.2}WO_4$. Importantly, as it is also clearly visible from Fig. 4 in ref. 37, ΔS_{mag} upon the HT-magnetic transition in the pristine $MnWO_4$ is well below R ln6. Even more, this value does not reach up to 30 K. Besides that, a well pronounced and broadened (*i.e.*, due to the cation mixture) anomaly at $T_{N2}^{c_p} \approx 10(1)$ K in our sample becomes especially clearly visible in the $c_{el}/T(T)$ presentation (inset to Fig. 6). It perfectly overlaps with the antiferromagnetic anomalies at T_{N1} = 13.4 K, T_{N2} = 12.5 K and T_{N3} = 7.4 K in $MnWO_4$,[38,39] stressing additionally the complexity of the magnetic structure of $Fe_{0.8}Mn_{0.2}WO_4$.

3.4 Electrical and thermal transport

The temperature dependence of electrical resistivity $\rho(T)$ for $Fe_{0.8}Mn_{0.2}WO_4$ is depicted in the inset to Fig. 7. It increases exponentially with decreasing temperature down to ≈300 K and then saturates, reaching the $\rho \approx 4.8$ kΩ m value. In the whole studied range, it is by ≈3–5 orders of magnitude higher than $\rho(T)$ reported for $CuFeS_2$ (*i.e.*, an impurity phase in our sample),[40] thus confirming the purity of the studied specimen.

Its comparison with the $\rho(T)$ of undoped $FeWO_4$ and $MnWO_4$ is presented in Fig. 7. As it is seen therein, all these dependencies can be nicely described by the Arrhenius approximation given as $\rho = \rho_0 e^{E_g/K_b T}$, where E_g is the energy gap. Interestingly, the latter value for $FeWO_4$ is reported to vary in a broad range of 150–260 meV.[4,15–17,41,42] Since the authors of ref. 4, 15 and 41 performed their studies on single crystalline materials obtained from chemical vapor transport reac-

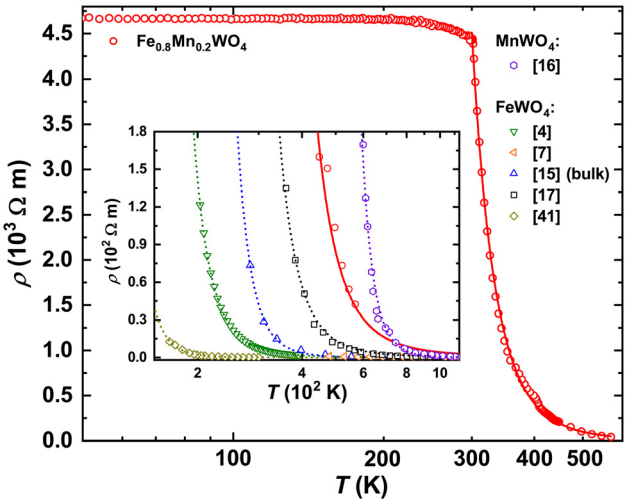

Fig. 7 The temperature dependence of electrical resistivity $\rho(T)$ for $Fe_{0.8}Mn_{0.2}WO_4$ together with the Arrhenius plot (red solid line). Inset: $\rho(T)$ for $Fe_{0.8}Mn_{0.2}WO_4$ in comparison with those of undoped $FeWO_4$ and $MnWO_4$. Dotted and solid lines correspond to the plots of the Arrhenius approximation.

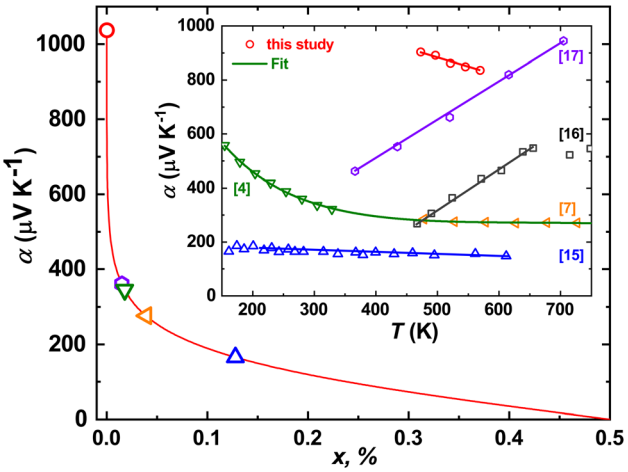

Fig. 8 Seebeck coefficient $\alpha_{300\ K}$ as a function of holes (Fe^{3+}) per Fe-site concentration (x) calculated from the Heikes equation (eqn (1)). Inset: temperature dependence of the Seebeck coefficient of thermopower $\alpha(T)$ for $Fe_{0.8}Mn_{0.2}WO_4$ in comparison with $FeWO_4$ [4,7,15,16] and $MnWO_4$ [17] samples of different origins.

tions and in ref. 16 and 17 bulk samples were studied, one has to conclude on the extreme sensitivity of $\rho(T)$ to any even minor impurities.

As it is discussed in ref. 41 and 43, Mn^{2+}-ions in $Fe_{1-x}Mn_xWO_4$ do not block the electron hopping paths, thus allowing charge carrier transfer also between chains, which results in the enhancement of $\rho(T)$. In agreement with this report, $Fe_{0.8}Mn_{0.2}WO_4$ reveals both higher electrical resistivity (Fig. 7) and an energy gap value of E_g = 310 meV (to be able to compare our value with the previously reported one, we performed an Arrhenius fit for the temperature range of 480–560 K). Importantly, the latter value is smaller than E_g = 705 meV of $MnWO_4$ [16] and larger than those observed for $FeWO_4$ (see the discussion above). Fitting $\rho(T)$ in the whole measured range of 300–560 K, one would obtain E_g = 247 meV for $Fe_{0.8}Mn_{0.2}WO_4$, clearly breaking the trend visible in Fig. 7. It is noteworthy that the band gap values deduced from $\rho(T)$ are always underestimated and the true E_g values for $MnWO_4$ and $FeWO_4$ deduced from spectroscopic measurements are 2.6–3 eV (ref. 7 and 18) and 2 eV,[18,19,44] respectively.

The Seebeck coefficients of thermopower $\alpha(T)$ of all $Fe_{1-x}Mn_xWO_4$-specimens studied up to now are positive in the whole temperature range, thus assuming the dominance of the hole-like conduction mechanism therein. Also, the $\alpha(T)$ of single crystalline $FeWO_4$ decreases nearly linearly with increasing temperature,[4,15,17] whereas for a bulk sample, an increase is reported[14] (Fig. 7). This is again an indication of the sensitivity of thermopower to the samples' crystallinity, similar to that discussed above for $\rho(T)$ dependencies. Interestingly, the $\alpha(T)$ of polycrystalline $FeWO_4$ [14] and $MnWO_4$ [16] (not shown in Fig. 8) reveal a change in the slope at a certain temperature, which is explained in both cases by the increase of the charge carrier mobilities. In line with these observations, the $\alpha(T)$ of single crystalline $Fe_{0.8}Mn_{0.2}WO_4$ decreases linearly with T. In the temperature range of ≈450–600 K, it is also the largest one [seemingly, the $\alpha(T)$ of $MnWO_4$ would become larger for T > 650 K].

Assuming now the $\alpha(T)$ of $Fe_{0.8}Mn_{0.2}WO_4$ to remain linear down to 300 K and the applicability of the simplified Heikes equation (*i.e.*, considering the degeneracy factors g_A and g_B to be equal)[45–47] given as:

$$\alpha = \frac{k_B}{e} \ln\left(\frac{1-x}{x}\right) \quad (1)$$

(where x is holes' concentration per site), we derived the $\alpha(x)$ dependence depicted in Fig. 8. Comparing $\alpha_{300\ K}$ = 1040 μV K^{-1} with such a plot, one obtains ≈0.002% of Fe^{3+} holes in the studied compound – a value, which is few orders of magnitude smaller than those reported for $FeWO_4$ of different origins. This finding is also in line with the performed structure refinement, confirming the studied specimen to be more stoichiometric in comparison with the pristine $FeWO_4$.

The temperature dependence of thermal conductivity $\kappa(T)$ for $Fe_{0.8}Mn_{0.2}WO_4$ is presented in Fig. 9. It is high for 5 K < T < 50 K (*e.g.*, by a factor of ≈3 higher than those of the high quality pyrite crystal[48]) and reveals a well pronounced maximum at T_{max} ≈ 12 K, which corroborates the good crystallinity and high quality of the sample. For T > 100 K, $\kappa(T)$ slightly increases almost linearly with temperature, which most probably occurs due to radiation heat losses (inset to Fig. 9).[49,50] Interestingly, two anomalies can be observed: (i) the increase of $\kappa_{ph}(T)$ that begins at T_{N1} = 67(1) K and (ii) an irregular behavior visible at $T_{N2}^{c_p}$ ≈ 8(1) K, in line with the specific heat measurements.

Since electrical resistivity for the studied mineral at 300 K is expected to be ≈12 kΩ m, the electronic component of $\kappa(T)$, in accordance with the Wiedemann–Franz law, would be $\kappa_{el}(300\ K) = L_0T/\rho = 6.1 \times 10^{-10}$ W m^{-1} K^{-1} ($L_0 = 2.44 \times 10^{-8}$ W

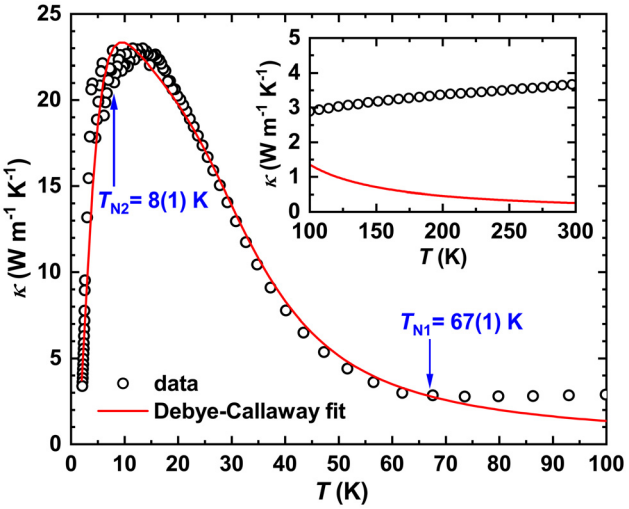

Fig. 9 Temperature dependence of thermal conductivity $\kappa(T)$ for $Fe_{0.8}Mn_{0.2}WO_4$ together with the fit to eqn (2). Inset: deviation of experimental data from the theoretical expectation due to radiation heat losses.

Ω K^{-2} is the Lorenz number). Comparing this κ_{el} with the values in Fig. 9, one can conclude that the $\kappa(T)$ of $Fe_{0.8}Mn_{0.2}WO_4$ is completely dominated by phonons (*i.e.*, κ_{ph}), and thus, obeys the Debye–Callaway model[51] given as:

$$\kappa_{ph} = \frac{{k_B}^4 T^3}{2\pi^2 v_S \hbar^3} \int_0^{\Theta_D/T} \frac{1}{{\tau_{tot}}^{-1}} \frac{x^4 e^x}{(e^x - 1)^2} dx \quad (2)$$

where

$${\tau_{tot}}^{-1} = {\tau_B}^{-1} + {\tau_{PD}}^{-1} + {\tau_N}^{-1} + {\tau_U}^{-1} \quad (3)$$

i.e., τ_{tot} is the sum of different scattering mechanisms including scattering of phonons on grain boundaries (τ_B) and point defects (τ_{PD}) as well as normal (τ_N) and umklapp (τ_U) phonon–phonon processes. The former two dominate the LT-range whereas the latter two dominate the HT-range.

The parameter Θ_D in eqn (2) denotes the Debye temperature of $Fe_{0.8}Mn_{0.2}WO_4$. It is rather impossible to deduce it from the above described $c_p(T)$; therefore we fitted the specific heat data for $ZnWO_4$ taken from ref. 9 in the T-range of 3–20 K to the $c_p(T) = \gamma T + \beta T^3 + \delta T^5$ ansatz, thus obtaining the Sommerfeld coefficient γ = 7.1(9) mJ mol^{-1} K^{-2}, β = 0.11(9) mJ mol^{-1} K^{-4} [corresponds to Θ_D ($ZnWO_4$) = 477(3) K] and δ = 4.1(9) × 10^{-4} mJ mol^{-1} K^{-6}. To obtain an approximate Debye temperature of $Fe_{0.8}Mn_{0.2}WO_4$, the value above was multiplied by $[M_r(ZnWO_4)/M_r(Fe_{0.8}Mn_{0.2}WO_4)]^{1/2}$ = 1.016, where M_r is the corresponding molar mass. Having now Θ_D ($Fe_{0.8}Mn_{0.2}WO_4$) = 485 K, we further calculate the velocity of sound for the studied mineral v_S = 3726 m s^{-1} using eqn (4) (therein n_{at} = 8.97 × 10^{28} m^{-3} is the concentration of atoms per unit cell volume).

$$v_S = \frac{k_B \Theta_D}{\hbar \sqrt[3]{6\pi^2 n_{at}}} \quad (4)$$

Table 3 Fit parameters (C_i) from the Debye–Callaway model (eqn (2)) together with the expression for the respective phonon scattering mechanisms from ref. 32

τ^{-1}	Equation	C_i	Units for C_i
${\tau_B}^{-1}$	$v_S/C1$	2.7(1)	[10^{-4} m]
${\tau_{PD}}^{-1}$	$C2x^4T^4$	183(4)	—
${\tau_N}^{-1}$	$C3xT^3$	5.96(9)	[10^5 s^{-1} K^{-3}]
${\tau_U}^{-1}$	$C4x^2T^3e^{(-\Theta_D/3T)}$	3.9(5)	[10^6 s^{-1} K^{-3}]

Introducing the Θ_D and v_S values in eqn (2), we fit $\kappa(T)$ in the temperature range of 1.8–106 K (Fig. 9) with an overall reliability factor R^2 = 0.993. The obtained parameters and their standard deviations are summarized in Table 3.

As one can see, the $C1$ coefficient indicates a rather large grain boundary size in agreement with the excellent microstructural quality of the studied single crystalline specimen. The $C2$ parameter, which is due to the point defects (*i.e.*, Mn-doping and/or the Fe^{3+}-holes), is approximately one order of magnitude smaller than single crystalline PbS[52] and polycrystalline indium thiospinels.[53] In the HT-range, we observe the contribution of both normal-($C3$) and umklapp ($C4$) phonon–phonon processes, as expected for single crystalline materials.

The discrepancies between the fit and experiment observed in the LT-region just below the maximum could be attributed to the features present in $c_p(T)$ (Fig. 5). To shed light on this problem, measurements performed on different samples with the same microstructure (*i.e.*, equal or similar τ_B and τ_{PD}) are necessary. Interestingly, the further mismatch of fit to eqn (4) to the experiment appears for $T > T_{N1}$ = 67(1) K. Obviously, to explain the $\kappa(T)$ behavior for the temperature range of 70–100 K, perturbation density functional theory (pDFT) calculations combined with additional experiments aiming at the estimation of phonon dispersions in $Fe_{0.8}Mn_{0.2}WO_4$ are required.

4 Conclusions

Combined X-ray powder diffraction (PXRD) and energy dispersive X-ray spectroscopic (EDXS) studies confirmed the natural crystal from the wolframite group originating from the Potosí province in Bolivia to be of high quality containing only local inclusions of chalcopyrite and some silicates. Its chemical formula was found to be $Fe_{1-x}Mn_xWO_4$ (x = 0.2). Further single crystal and powder XRD experiments confirmed the mineral to crystallize with the monoclinic wolframite structure type. A slight monoclinic distortion is clearly evidenced by the split of hkl reflections with $h \neq 0$ and $l \neq 0$ in the PXRD patterns.

The measurements of the temperature and field-dependent magnetic susceptibility for $Fe_{1-x}Mn_xWO_4$ (x = 0.2) indicated an effective magnetic moment close to that expected for Fe^{2+} ions. A complex magnetic structure with transitions at T_{N1} = 67(1) K and T_{N2} = 28(3) K is also in line with the earlier studied quaternary wolframites. Further confirmation of this complexity is deduced from specific heat measurements revealing anomalies

at $T_{N1}^{C_p}$ = 66(1) K and $T_{N2}^{C_p}$ = 8(1) K. It is noteworthy that the reduced magnetic entropy of $\approx R \ln 3$ (instead of $R \ln 5$) upon the HT transition indicates the failure of the simplified LS-coupling scheme in the description of the magnetism in the studied mineral.

The electrical resistivity of $Fe_{1-x}Mn_xWO_4$ (x = 0.2) increases exponentially upon decreasing temperature reaching a saturation value of $\rho \approx 4.8$ kΩ m below 300 K. The high-temperature energy gap of 310 meV, deduced from the exponential decrease with temperature, is expectedly closer to $FeWO_4$ (150–260 meV) than to $MnWO_4$ (710 meV).

The measured thermal conductivity slightly decreases with decreasing temperature down to $T_{N1} \approx 66(1)$ K and then overcomes a huge maximum centered at $T_{max} \approx 12$ K, revealing some additional anomaly at $T_{N2}^{C_p} \approx 8(1)$ K. Assuming it to be dominated by the phonon processes [the electronic contribution to $\kappa(T)$ is found to be $\approx 10^{-10}$ W m^{-1} K^{-1}], the Debye–Callaway model was applied. Such a fit indicated enlarged grain boundary sizes, enhanced defect concentration and the dominance of umklapp processes in the studied single crystal.

Data availability

The data supporting this article have been included as part of the ESI.†

Conflicts of interest

There are no conflicts of interest to declare.

Acknowledgements

The QD DynaCool-12 measurement system was acquired within the DFG project 422219907. We thank S. Kostmann and U. Burkhardt for performing EDX characterization of our sample and H. Borrmann, E. Meier and A. Schwarzer for their assistance during XRD measurements. V. L. is grateful to DFG for financial support (project 467257848).

References

1 D. Diaz-Anichtchenko, J. E. Aviles-Coronado, S. López-Moreno, R. Turnbull, F. J. Manjón, C. Popescu and D. Errandonea, *Inorg. Chem.*, 2024, **63**, 6898–6908.
2 O. Fabelo, J. Gonzalez-Platas, S. Savvin, P. Botella and D. Errandonea, *J. Appl. Phys.*, 2024, **136**, 175901.
3 S. G. Altendorf, D. Takegami, A. Meléndez-Sans, C. F. Chang, M. Yoshimura, K. D. Tsuei, A. Tanaka, M. Schmidt and L. H. Tjeng, *Phys. Rev. B*, 2023, **108**, 085119.
4 A. Maignan, M. Schmidt, Y. Prots, O. I. Lebedev, R. Daou, C.-F. Chang, C.-Y. Kuo, Z. Hu, C.-T. Chen, S.-C. Weng, S. G. Altendorf, L.-H. Tjeng and Y. Grin, *Chem. Mater.*, 2022, **34**, 789–797.
5 M. Assis, A. C. Tello, F. S. Abud, P. Negre, L. K. Ribeiro, R. A. Ribeiro, S. H. Masunaga, A. E. Lima, G. E. Luz Jr, R. F. Jardim, A. B. Silva, J. Andrés and E. Longo, *Appl. Surf. Sci.*, 2022, **600**, 154081.
6 D. A. Umbsaar and S. M. Antao, *Minerals*, 2021, **12**, 42.
7 R. Schuler, F. Bianchini, T. Norby and H. Fjellvåg, *ACS Appl. Mater. Interfaces*, 2021, **13**, 7416–7422.
8 B. Huang and J. N. Hart, *Phys. Chem. Chem. Phys.*, 2020, **22**, 1727–1737.
9 W. G. Lyon and E. F. Westrum, *J. Chem. Thermodyn.*, 1974, **6**, 763–780.
10 R. O. Keeling, *Acta Crystallogr.*, 1957, **10**, 209–213.
11 E. García-Matres, N. Stüßer, M. Hofmann and M. Reehuis, *Eur. Phys. J. B*, 2003, **32**, 35–42.
12 G. Lautenschläger, H. Weitzel, T. Vogt, R. Hock, A. Böhm, M. Bonnet and H. Fuess, *Phys. Rev. B: Condens. Matter Mater. Phys.*, 1993, **48**, 6087–6098.
13 I. Urcelay-Olabarria, J. M. Perez-Mato, J. L. Ribeiro, J. L. García-Muñoz, E. Ressouche, V. Skumryev and A. A. Mukhin, *Phys. Rev. B: Condens. Matter Mater. Phys.*, 2013, **87**, 014419.
14 H. Obermayer, H. Dachs and H. Schröcke, *Solid State Commun.*, 1973, **12**, 779–784.
15 E. Schmidbauer, U. Schanz and F. J. Yu, *J. Phys.: Condens. Matter*, 1991, **3**, 5341–5352.
16 R. Bharati, R. Singh and B. Wanklyn, *J. Phys. Chem. Solids*, 1982, **43**, 641–644.
17 R. Bharati, Y. P. Yadava and R. A. Singh, *J. Mater. Sci. Lett.*, 1983, **2**, 808–810.
18 T. Ejima, T. Banse, H. Takatsuka, Y. Kondo, M. Ishino, N. Kimura, M. Watanabe and I. Matsubara, *J. Lumin.*, 2006, **119–120**, 59–63.
19 S. Rajagopal, V. Bekenev, D. Nataraj, D. Mangalaraj and O. Khyzhun, *J. Alloys Compd.*, 2010, **496**, 61–68.
20 K. Hoang, *Phys. Rev. Mater.*, 2017, **1**, 024603.
21 D. Errandonea and J. Ruiz-Fuertes, *Crystals*, 2018, **8**, 71.
22 R. Guillen and J. R. Regnard, *Phys. Chem. Miner.*, 1985, **12**, 246–254.
23 T. Birkett, *Can. Mineral.*, 2003, **41**, 1296–1297.
24 *STOE Powder Software, WinXPow (version 2)*, STOE and Cie GmbH, Darmstadt, 2001.
25 L. Akselrud and Y. Grin, *J. Appl. Crystallogr.*, 2014, **47**, 803–805.
26 P. J. Withers, *Rep. Prog. Phys.*, 2007, **70**, 2211–2264.
27 N. Rossini, M. Dassisti, K. Benyounis and A. Olabi, *Mater. Des.*, 2012, **35**, 572–588.
28 P. Withers and H. Bhadeshia, *Mater. Sci. Technol.*, 2001, **17**, 355–365.
29 A. Nezu, H. Matsuzaka and R. Yokoyama, *Rigaku J.*, 2014, **30**, 4–12.
30 C. Escobar, H. Cid-Dresdner, P. Kittl and I. Dümler, *Am. Mineral.*, 1971, **56**, 489–498.
31 D. Ülkü, *Z. Kristallogr. Krist.*, 1967, **124**, 192–219.

32 J. Emsley, *The Elements*, Clarendon Press, Oxford, 3rd edn, 1998.
33 M. Almeida, L. Cavalcante, C. Morilla-Santos, P. L. Filho, A. Beltrán, J. Andrés, L. Gracia and E. Longo, *Mater. Charact.*, 2012, **73**, 124–129.
34 H. Weitzel, *Solid State Commun.*, 1969, **7**, 1249–1252.
35 M. A. P. Almeida, L. S. Cavalcante, C. Morilla-Santos, C. J. Dalmaschio, S. Rajagopal, M. S. Li and E. Longo, *CrystEngComm*, 2012, **14**, 7127–7132.
36 Y.-X. Zhou, H.-B. Yao, Q. Zhang, J.-Y. Gong, S.-J. Liu and S.-H. Yu, *Inorg. Chem.*, 2009, **48**, 1082–1090.
37 C. P. Landee and E. F. Westrum, *J. Chem. Thermodyn.*, 1976, **8**, 663–674.
38 C. P. Landee, J. Westrum and F. Edgar, *AIP Conf. Proc.*, 1976, **29**, 445–446.
39 C. M. N. Kumar, Y. Xiao, P. Lunkenheimer, A. Loidl and M. Ohl, *Phys. Rev. B: Condens. Matter Mater. Phys.*, 2015, **91**, 235149.
40 P. Wyżga, M. Bobnar, C. Hennig, A. Leithe-Jasper, T. Mori and R. Gumeniuk, *Z. Anorg. Allg. Chem.*, 2017, **643**, 858–863.
41 K. Sieber, K. Kourtakis, R. Kershaw, K. Dwight and A. Wold, *Mater. Res. Bull.*, 1982, **17**, 721–725.
42 Y. Noda, M. Shimada, M. Koizumi and F. Kanamaru, *J. Solid State Chem.*, 1979, **28**, 379–384.
43 K. Sieber, H. Leiva, K. Kourtakis, R. Kershaw, K. Dwight and A. Wold, *J. Solid State Chem.*, 1983, **47**, 361–367.
44 W. S. Choi, K. Taniguchi, S. J. Moon, S. S. A. Seo, T. Arima, H. Hoang, I.-S. Yang, T. W. Noh and Y. S. Lee, *Phys. Rev. B: Condens. Matter Mater. Phys.*, 2010, **81**, 205111.
45 J. Robert, R. Heikes and R. W. Ure, *Thermoelectricity: Science and Engineering*, Interscience Publishers, New York - London, 1961.
46 J.-S. Zhou and J. B. Goodenough, *Phys. Rev. B: Condens. Matter Mater. Phys.*, 1999, **60**, R15002–R15004.
47 P. M. Chaikin and G. Beni, *Phys. Rev. B*, 1976, **13**, 647–651.
48 E. Zuñiga-Puelles, R. Cardoso-Gil, M. Bobnar, I. Veremchuk, C. Himcinschi, C. Hennig, J. Kortus, G. Heide and R. Gumeniuk, *Dalton Trans.*, 2019, **48**, 10703–10713.
49 K. A. Borup, J. de Boor, H. Wang, F. Drymiotis, F. Gascoin, X. Shi, L. Chen, M. I. Fedorov, E. Müller, B. B. Iversen and G. J. Snyder, *Energy Environ. Sci.*, 2015, **8**, 423–435.
50 *Thermal transport option user's manual*, Quantum design, Inc. 6325 Lusk Blvd., San Diego, CA, USA technical report, 2002.
51 T. M. Tritt, Thermal Conductivity: Theory, Properties, and Applications, Springer New York, NY, 2004.
52 E. Zuñiga-Puelles, V. Levytskyi, A. Özden, T. Gürel, N. Bulut, C. Himcinschi, C. Sevik, J. Kortus and R. Gumeniuk, *Phys. Rev. B*, 2023, **107**, 195203.
53 E. Zuñiga-Puelles, A. Özden, V. Pacheco, L. Akselrud, R. Cardoso-Gil, A. Straßheim, P. Wyżga, C. Himcinschi and R. Gumeniuk, *J. Alloys Compd.*, 2024, **976**, 173055.